RSC Advances

ROYAL SOCIETY OF CHEMISTRY

www.rsc.org/advances

Preparation and heavy-ion irradiation effects of $Gd_2Ce_xZr_{2-x}O_7$ ceramics

Xirui Lu[1,2], Yi Ding[2], Xiaoyan Shu[2], Xueli Mao[2], Xiaolin Wang[1*]

[1]*China Academy of Engineering Physics, Mianyang 621900, P. R. China*

[2]*Key Subject Laboratory of National Defense for Radioactive Waste and Environmental Security, Southwest University of Science and Technology, Mianyang 621010, P. R. China*

Abstract: A number of compositions with general stoichiometry of $Gd_2Ce_xZr_{2-x}O_7$ ($0 \le x \le 2$) ceramics have been synthesized and received irradiation test at room temperature with Xe^{20+} ions in a broad fluence range. X-ray diffraction (XRD) measurements shows that $Gd_2Ce_xZr_{2-x}O_7$ ($0 \le x \le 0.2$) samples adopt the pyrochlore structure, whereas $Gd_2Ce_xZr_{2-x}O_7$ ($0.2 \le x \le 2.0$) samples predominantly displayed an anion deficient fluorite structure, indicating that the structures of $Gd_2Ce_xZr_{2-x}O_7$ are determined by the content of doped Ce^{4+} ion. XRD results of irradiated samples ($Gd_2Zr_2O_7$, $Gd_2Ce_2O_7$) indicate that $Gd_2Zr_2O_7$ was transformed into a radiation resistant anion deficient fluorite structure with increasing fluence, whereas the $Gd_2Ce_2O_7$ was partially amorphized. It was found that the structural evolutions induced by irradiation are strongly dependent on the samples composition and ions fluence. In addition, SEM results show that the density and hardness of waste forms play an important role in the morphology modifications induced by irradiation. These results would be considered for design and elaboration of future matrices for actinide immobilization or transmutation.

Keywords

Heavy ion irradiation; Pyrochlore; X-ray diffraction; Structure; Morphology

1. Introduction

Zirconate pyrochlores are one of the candidate materials proposed for immobilizing

* Corresponding author. Tel./fax: +86 816 2483157.
E-mail address: xlwang@caep.cn

actinide wastes. They have been considered as a key component in synroc-based pyrochlore ceramics for geological immobilization of surplus Pu in the US [1]. It is very important that suitable waste form materials should be radiation resistant in geological repository. During long term storage, nuclear waste forms are submitted to severe radiations which induce atomic rearrangements. These structural modifications lead to the deterioration of physic-chemical properties of waste form materials.

The pyrochlores under consideration in this study typically exhibit the $A_2B_2O_7$ stoichiometry, where actinides or lanthanides can be incorporated into the eight-coordinated A-site and metals occupy the six-coordinated B-site. Ordered $A_2B_2O_7$ pyrochlores belong to the Fd-3m space group, which is a superstructure of the ideal fluorite structure (Fm-3 space group) with twice the lattice constant. A and B cations occupy the 16c (0,0,0) and 16d (0.5,0.5,0.5) sites, respectively, and oxygens are located at the 48f (x,0.125,0.125) and 8b (0.375,0.375,0.375) positions (using Wyckoff notation). The anion sublattice can be completed by adding missing oxygens in the 8a site to form the anion-deficient fluorite structure. It is well known that the stability of pyrochlore structure is governed by the ratio of the ionic radii of A and B cation (r_A/r_B). The range of pyrochlore stability extends from 1.46 for $Gd_2Zr_2O_7$ to 1.78 for $Sm_2Ti_2O_7$. For smaller ionic radii ratios, $r_A/r_B < 1.46$, anion-deficient fluorite is a stable structure, whilst the monoclinic structure is stable for ionic radii ratios $r_A/r_B > 1.78$ [2, 3].

Given that nuclear waste forms will be subject to considerable α-recoil radiation damage in geological repository, it is important to understand effect of radiation on the pyrochlore structure. Considerable work has been carried out to investigate the radiation induced crystalline to amorphous transformation in pyrochlore [1, 4-6]. However, information concerning the damage induced by electronic excitation arising from irradiation with

heavy-ion is still incomplete, only a small number of studies devoted to this topic [7-10]. One of the main results is that the susceptibility to radiation-induced amorphization exhibits a systematic decrease with increasing Zr content. $Gd_2Zr_2O_7$ is transformed into a radiation resistant anion-deficient fluorite structure upon irradiation at room temperature, whereas $Gd_2Ti_2O_7$ is readily amorphized. From these results, it was concluded that zirconates are more radiation resistant than titanates. Radiation damage resulting from alpha-decay events of the immobilized radionuclides may cause significant microstructural changes, macroscopic swelling and a decrease of chemical durability of waste forms [11]. For example, $Gd_2Ti_2O_7$, one of the primary waste forms being considered, undergoes an irradiation induced amorphization by either alpha-decay damage or heavy ions irradiations at a relatively low dose of about 0.18 displacements per atom (dpa), which cause a factor 50 increase in the dissolution rate of Pu [12-15]. However, $Gd_2(Ti_{1-x}Zr_x)_2O_7$ with higher Zr contents have shown remarkable resistance to irradiation induced amorphization, because these compositions readily disorder on the A and B sites forming a defect fluorite structure [16]. The increasing radiation ‘‘resistance’’ with increasing Zr content in the $Gd_2(Ti_{1-x}Zr_x)_2O_7$ system illustrates the important effect of the B site cations.

This paper reports detailed characterization of the as-prepared crystalline $Gd_2Ce_xZr_{2-x}O_7$ family of pyrochlores for x = 0-2, whose ionic radii ratios range from r_A/r_B = 1.21 (x = 2, $Gd_2Ce_2O_7$) to r_A/r_B = 1.46 (x = 0, $Gd_2Zr_2O_7$), along with characterization of the structural and morphology modifications associated with irradiation with 2 MeV Xe^{20+} ions at various fluences from 1×10^{13} to 1×10^{16} ions/cm^2.

2. Experimental

Pyrochlore pellets with various solubility of Ce^{4+} were prepared by a standard solid state process in air. Stoichiometric amounts of Gd_2O_3, ZrO and CeO_2 oxides were intimately mixed in ethanol using a ball-mill and subsequently dried. After drying, the powders were isostatically pressed into pellets at 10 MPa. The obtained pellets were sintered at 1500 °C for 72 h. Pellets were polished to a mirror finished using 0.5 μm diamond lapping films.

Pyrochlore oxides pellets were irradiated at room temperature with 2 MeV Xe^{20+} ions at the heavy ion research facility in Lanzhou at fluences from 1×10^{13} up to 1×10^{16} ions/cm^2.

The surface morphology of samples was charactered by scanning electron microscope (SEM, Ultra 55, Carl Zeiss AG, Germany). Microstructural evolution upon ion irradiation has been examined by transmission electron microscopy (TEM). The TEM samples were prepared by dispersing the powdered samples on holey-carbon Cu grids. XRD experiments were carried out on a Bruker D8 diffractometer using Cu Kα radiation, in an 2θ angular range of 10-100^o, with a step size of 0.02^o and a counting time of 20 s per step. The XRD patterns were analyzed by Rietveld refinement and Le Bail refinement methods using Fullprof-2k software package [17].

The diffraction patterns were analyzed using two different methods. In the first method, the amorphous fraction f_A was deduced from the net areas of the corresponding XRD lines by using the following equation:

$$f_A = 1 - \frac{\sum_{i=1}^{n} \frac{A_i^{irradiated}}{A_i^{unirradiated}}}{n} \qquad (1)$$

Where $A_i^{irradiated}$ and $A_i^{unirradiated}$ are the areas of the ith XRD line in the pattern recorded on irradiated and unirradiated samples, respectively, and n is number of lines considered. Pseudo-Voigt profiles were used to fit the diffraction peaks. In the second one, the diffraction

patterns were analyzed by Rietved refinement using the GSAS package [18], with a procedure described by Wuensch et al. [19] in order to determine the fraction of anion-deficient fluorite structure induced by irradiation (which coexists with the remaining pyrochlore phase).

The densities of the samples were measured by Archimedes method. Vickers hardness of samples was evaluated with a Vickers indentation machine (Akashi AVK, Japan) at least six indents under 5 Kg.

3 Results and Discussion

3.1. Unirradiated $Gd_2Ce_xZr_{2-x}O_7$ ($0 \le x \le 2$)

Characterizations of the long range structure of $Gd_2Ce_xZr_{2-x}O_7$ samples were carried out using X-ray diffraction. Fig. 1 shows the XRD patterns of the $Gd_2Ce_xZr_{2-x}O_7$ ($0 \le x \le 2$) samples. Ordered $A_2B_2O_7$ pyrochlores belong to Fd-3m space group which is a superstructure of the ideal fluorite structure (Fm-3m space group) with twice the lattice constant. A and B cations occupy the 16c and 16d sites, respectively, and oxygens are located at the 48f and 8b positions. The anion sublattice can be completed by adding missing oxygens in the 8a site to form the fluorite structure. As shown in Fig. 1, for $Gd_2Zr_2O_7$, the characteristic superstructure diffraction peaks of pyrochlore structure are observed. However, with the increase of Ce^{4+} (compositions from $Gd_2Ce_{0.2}Zr_{1.8}O_7$ to $Gd_2Ce_2O_7$), the superstructure peaks disappear. This indicates that a phase transformation from ordered pyrochlore (Fd-3m) to anion deficient fluorite (Fm3m) structure occurred. It can be also found that the diffraction peaks shift to low angles with increasing Ce^{4+}. The calculated unit cell parameter *a* and cell volume slightly increased from 0.52875 to 0.543 nm, 0.14783 to 0.16010 nm^3, respectively, from $Gd_2Ce_{0.2}Zr_{1.8}O_7$ to the composition $Gd_2Ce_2O_7$, and the details are listed in Table 1. Furthermore, as shown in Fig. 2, the calculated XRD pattern gives a perfect fit to the observed based on the Rietveld refinement. This lattice expansion may due to larger ionic

radii of Ce^{4+}, 0.87 Å (six coordinate), than that of Zr^{4+}, 0.72 Å (six coordinate).

3.2. 2 MeV Xe^{20+} irradiations

3.2.1 Microstructural evolution and irradiation tolerance of $Gd_2Zr_2O_7$ under irradiation with various fluences

Fig. 3 shows the XRD patterns of $Gd_2Zr_2O_7$ after irradiating with 2 MeV Xe^{20+} ions at fluences ranging from 1×10^{13} up to 1×10^{16} ions/cm^2. The diffraction reflections related to the supercell of the pyrochlore structure disappear at 1×10^{14} ions/cm^2, and only the reflections corresponding to fluorite structure remain observed (Fig. 3a). This indicates that heavy ion irradiation has induced an order to disorder phase transition: $Gd_2Zr_2O_7$ is transformed into an anion-deficient fluorite structure by disordering of cations occupying the A and B sites. In addition, it was found that the diffraction peaks shift to low angle with increasing fluences 1×10^{13} to 1×10^{16} ions/cm^2. This indicates that the values of d spacing of reflection increase. The calculated unit cell parameter *a* and cell volume slightly increased from 1.05287 to 1.05397 nm, 1.16714 to 1.17080 nm^3, respectively, before and after irradiation with 2 MeV Xe^{20+} ions at increasing fluences, and the details are listed in Table 2. Fig. 4 shows the results of the Rietveld fit for the virgin and highest irradiated samples. As can be seen in Fig. 3b, a broad peak becomes visible around $2\theta = 28.4^{o}$ and no additional broad peak appearing above 1×10^{13} ions/cm^2. This broad peak arises from the diffuse scattering due to the formation of an amorphous phase [20]. In order to determine the amorphous extent of $Gd_2Zr_2O_7$ quantitatively under different irradiation fluence, we calculated the relative amorphous fraction of $Gd_2Zr_2O_7$. Fig. 5 shows the variation of amorphous fractions versus the ion fluences. The results show that the amorphous fractions increase with increasing ion fluences. This is consistent with the results reported by Li [21]. The observed increase in the XRD peak width of these reflections after irradiation in Fig. 3(a) may due either to “particle size broadening” or “strain broadening” [22,23]. Assuming the broadening is due to the particle size effect, according to

Scherrer's formula [22], the particle size in the implanted layer is estimated to be about 461 nm at fluence of 1×10^{16} ions/cm^2. This suggests that the average grain size in the implanted layers is significantly smaller than that of the unirradiated samples 762 nm. Furthermore, ion implantation can also induce large near surface compressive biaxial stress states, so the non-uniformity of strain produced by the compressive biaxial stress probably also contributes to the observed peak broadening [23]. Microstructural evolution upon ion irradiation has been examined by HRTEM. No ion irradiation-induced amorphization was observed for $Gd_2Zr_2O_7$, as shown in Fig. 6. Thus, the $Gd_2Zr_2O_7$ with pyrochlore structure is more stable during irradiation due to the potential for disordering on the A and B sites.

3.2.2 Microstructural evolution and irradiation tolerance of $Gd_2Ce_2O_7$ under irradiation with various fluences

Fig. 7 shows XRD patterns recorded on $Gd_2Ce_2O_7$ before and after irradiation with 2 MeV Xe^{20+} ions at increasing fluences. As can be seen in Fig. 7, the amorphous fractions increase with increasing ion fluences. This is also consistent with the results reported by Li [21]. Furthermore, it was found that the diffraction peaks shift to low angle with increasing fluences 1×10^{13} to 1×10^{16} ions/cm^2. This indicates that the values of d spacing of reflection increase. The calculated unit cell parameter *a* and cell volume slightly increased from 1.06306 to 1.06721 nm, 1.20146 to 1.21549 nm^3, respectively, before and after irradiation with 2 MeV Xe^{20+} ions at increasing fluences, and the details are listed in Table 3. Fig. 8 shows the results of the Rietveld fit for the virgin and highest irradiated samples. As can be seen in Fig. 7, it was found that the XRD peak width of these reflections increase after irradiation. It may be also due either to "particle size broadening" or "strain broadening". Fig. 9 shows the HRTEM images of $Gd_2Ce_2O_7$ before and after irradiated by 2 MeV Xe^{20+} ions at fluence of 1×10^{16} ions/cm^2. As can be seen in Fig. 9b, amorphous features were observed in some grains of

$Gd_2Ce_2O_7$ irradiated by 2 MeV Xe^{20+} ions at fluence of 1×10^{16} ions/cm^2. These indicate that $Gd_2Ce_2O_7$ is partly amorphized after irradiated by 2 MeV Xe^{20+} ions at fluence of 1×10^{16} ions/cm^2.

3.2.3. Micromorphology modification and irradiation tolerance of $Gd_2Zr_2O_7$ and $Gd_2Ce_2O_7$ under irradiation with various fluences

In order to investigate the micromorphology modification and tolerance of waste forms, the surface morphology of samples irradiated with various fluences were characterized using SEM. Fig. 10. shows SEM images of $Gd_2Zr_2O_7$ and $Gd_2Ce_2O_7$ irradiated with 2 MeV Xe^{20+} ions at various fluences. As can be seen in Fig. 10(a), the surface morphology of unirradiated $Gd_2Zr_2O_7$ sample is flat and smooth. However, the surface morphology become porous and the grain boundary damaged after irradiated with 2 MeV Xe^{20+} ions at fulence of 1×10^{16} ions/cm^2 (see Fig. 10(b)). This micromorphology evolution may be due to the interfaces between the grain boundaries and pores are more susceptible to being damaged by the incident ions. For $Gd_2Ce_2O_7$ samples, the flat and smooth surface (see Fig. 8(c)) only become rough (see Fig. 10(d)) after irradiated with 2 MeV Xe^{20+} ions at fulence of 1×10^{16} ions/cm^2. The grain boundary dissolution and porousness were not markedly increased, which indicate that $Gd_2Ce_2O_7$ have better irradiation tolerance. It was found that the density of $Gd_2Ce_2O_7$ and $Gd_2Zr_2O_7$ are 6.519 and 6.310 g/cm^3, respectively. Furthermore, the hardness of $Gd_2Ce_2O_7$ and $Gd_2Zr_2O_7$ are 1074 and 698.1 kg/mm^2, respectively. Hence, we speculate that the better irradiation tolerance of $Gd_2Ce_2O_7$ may due to their higher density and hardness. The results suggest that the irradiation stability of waste forms is strongly dependent on the density and hardness.

4. Conclusion

$Gd_2Ce_xZr_{2-x}O_7$ ($0\leq x\leq 2$) waste forms with single phase structure have been successfully

synthesized. It was found that the structures of unirradiated $Gd_2Ce_xZr_{2-x}O_7$ are determined by the solubility of Ce^{4+}. The pyrochlore structure was transformed into fluorite structure with increasing Ce^{4+}. In addition, pyrochlore pellets with $Gd_2Zr_2O_7$ and $Gd_2Ce_2O_7$ composition were irradiated with 2 MeV Xe^{20+} ions in a broad fluence range (from 1×10^{13} up to 1×10^{16} ions/cm^2) in order to investigate the structural and morphological modifications induced by irradiation. The results indicate that $Gd_2Zr_2O_7$ was transformed into a radiation resistant anion deficient fluorite structure irradiated with 2 MeV Xe^{20+} ions at various fluences from 1×10^{13} to 1×10^{16} ions/cm^2. However, for $Gd_2Ce_2O_7$, amorphization occur. It was found that the structural modifications induced by irradiation with heavy ions at various fluences are strongly dependent on the samples composition and ions fluence. SEM results show that the density and hardness of waste forms play an important role in the morphology modifications induced by irradiation. This work will be useful in designing new and better waste forms for immobilizing radioactive waste.

Acknowledgement

This work was supported by the National Natural Science Foundation of China (No. 41302028; 41272050), China Postdoctoral Science Foundation Funded Project (No. 2014M552384) and the Open Foundation of Joint Laboratory for Extreme Conditions Matter Properties, Southwest University of Science and Technology and Research Center of Laser Fusion, CAEP (No. 12zxjk04).

References

[1] B.D Begg, N.J Hess, D.E McCready, S. Thevuthasan, W.J Weber, J. Nucl. Mater. 289 (2001) 188.

[2] R.C. Ewing, W.J. Weber, J. Lian, Journal of Applied Physics, 95 (2004) 5949.

[3] M.A. Subramanian, G. Aravamudan, G.V.S. Rao, Prog. Sol. State Chem. 15 (1983) 55.

[4] K.E. Sickafus, R.W. Grimes, J.A. Valdez, A. Cleave, M. Tang, M. Ishimaru, S.M.Corish, C.R. Stanek, B.P. Uberuaga, Nat. Mater. 6 (2007) 217.

[5] J. Lian, L. Wang, J. Chen, K. Sun, R.C. Ewing, J.M. Farmer, L.A. Boatner, Acta Mater. 51 (2003) 1493.

[6] J. Lian, L.M. Wang, S.X. Wang, J. Chen, L.A. Boatner, R.C. Ewing, Phys. Rev. Lett. 87 (2001) 145901.

[7] M.K. Patel, V. Vijayakumar, S. Kailas, D.K. Avasthi, J.C. Pivin, A.K. Tyagi, J. Nucl. Mater. 380 (2008) 93.

[8] G. Sattonnay, S. Moll, M. Hebst-Ghysel, L. Thomé, F. Garrido, J.-M. Costantini, C. Trautmann, Nucl. Instr. and Meth. B 266 (2008) 3043.

[9] M. Lang, J. Lian, J. Zhang, F. Zhang, W.J. Weber, C. Trautmann, R.C. Ewing, Phys. Rev. B 79 (2009) 224105.

[10] M. Lang, F.X. Zhang, R.C. Ewing, J. Lian, C. Trautmann, Z. Wang, J. Mater. Res. 24 (2009) 1322.

[11] W.J. Weber, R.C. Ewing, C.R.A. Catlow, T. Diaz de la Rubia, L.W. Hobbs, C. Kinoshita, Hj. Matzke, A.T. Motta, M. Nastasi, E.K.H. Salje, E.R. Vance, S.J. Zinkle, J. Mater. Res. 13 (1998) 1434.

[12]W.J. Weber, F.P. Roberts, Nucl. Technol. 60 (1983) 178.

[13] S.X. Wang, L.M. Wang, R.C. Ewing, G.S. Was, G.R. Lumpkin, Nucl. Instr. and Meth. B 148 (1999) 704.

[14] W.J. Weber, J.W. Wald, Hj. Matzke, Mater. Lett. 3 (1985) 173.

[15] W.J. Weber, J.W. Wald, Hj. Matzke, J. Nucl. Mater. 138 (1986) 196.

[16] W.J. Weber, R.C. Ewing, Mater. Res. Soc. Symp. Proc.713 (2002) 443.

[17] J. Rodriguez-Carvajal, Multi pattern Rietveld refinement program, Fullprof. 2K Version 1.6, July 2000.

[18] A.C. Larson, R.B. Von Dreele, General Structure Analysis System, LANSCE, Los Alamos National Laboratory, Report LAUR 86-748, 1994.

[19] B.J. Wuensch, K.W. Eberman, C. Heremans, E.M. Ku, P. Onnerud, E.M.E. Yeo, S.M. Haile, J.K. Stalick, J.D. Jorgensen, Solid State Ionics 129 (2000) 111.

[20] G Sattonnay, N Sellami, L Thomé, C. Legros, C. Grygiel, I. Monnet, J. Jagielski, I. Jozwik-Biala, P. Simon, Acta Materialia, 61(2013) 6492.

[21] Y.H Li, Y.Q Wang, M. Zhou, C.P Xu, J.A Valdez, K.E Sickafus, Nucl. Instrum. Meth. B 269(2011) 2001.

[22] B.D. Cullity, Elements of X-Ray Diffraction, Addison-Wesley Publishing Company Inc., 1978.

[23] A. Misra, S. Fayeulle, H. Kung, T.E. Mitchell, M. Nastasi, Nucl. Instrum. Meth. B 148 (1999) 211.

Figure Captions

Fig. 1. XRD patterns of some of the compositions in $Gd_2Ce_xZr_{2-x}O_7$. The peaks corresponding to the supercell of the pyrochlore structure are noted with a star.

Fig. 2. Rietveld refinement results of powder X-ray diffraction of (a) $Gd_2Zr_2O_7$ and (b) $Gd_2Ce_2O_7$.

Fig. 3. (a) Evolution with the ion fluence of XRD patterns of $Gd_2Zr_2O_7$ irradiated with 2 MeV Xe^{20+} ions; (b) zoom of the 25-35° region. The peaks corresponding to the supercell of the pyrochlore structure are noted with a star.

Fig. 4. Rietveld refinement results of powder X-ray diffraction of $Gd_2Zr_2O_7$ (a) virgin and (b) irradiated with 2 MeV Xe^{20+} at fluences of 1×10^{16} ions/cm^2

Fig. 5. Relative amorphous fraction of the samples irradiated at various fluences

Fig. 6. HRTEM images of $Gd_2Zr_2O_7$ irradiated by 2 MeV Xe^{20+} ions at different fluences: (a) unirradiated; (b) 1×10^{16} ions/cm^2

Fig. 7. (a) Evolution with the ion fluence of XRD patterns of $Gd_2Ce_2O_7$ irradiated with 2 MeV Xe^{20+} ions; (b) zoom of the 25-35° region.

Fig. 8. Rietveld refinement results of powder X-ray diffraction of $Gd_2Ce_2O_7$ (a) virgin and (b) irradiated with 2 MeV Xe^{20+} at fluences of 1×10^{16} ions/cm^2

Fig. 9. HRTEM images of $Gd_2Ce_2O_7$ irradiated by 2 MeV Xe^{20+} ions at different fluences: (a) unirradiated; (b) 1×10^{16} ions/cm^2

Fig. 10. SEM images of samples: (a) $Gd_2Zr_2O_7$ and (c) $Gd_2Ce_2O_7$ unirradiated; (b) $Gd_2Zr_2O_7$

and (d) $Gd_2Ce_2O_7$ irradiated with 2 MeV Xe^{20+} at fluences of 1 × 10^{16} ions/cm^2

Table 1. Phase structure and lattice parameter *a* and cell volume determined from Rietveld refinement performed on XRD patterns of $Gd_2Ce_xZr_{2-x}O_7$ samples

Sample	Phase	*a* (nm)	*α* (°)	*V* (nm^3)
PDF00-016-0799	Pyrochlore	1.05010	90	1.15796
PDF01-080-0471	Fluorite	0.52636	90	0.14583
$Gd_2Zr_2O_7$	Pyrochlore	1.05329	90	1.16854
$Gd_2Zr_{1.8}Ce_{0.2}O_7$	Fluorite	0.52875	90	0.14783
$Gd_2Zr_{1.6}Ce_{0.4}O_7$	Fluorite	0.52977	90	0.14868
$Gd_2Zr_{1.4}Ce_{0.6}O_7$	Fluorite	0.53251	90	0.15100
$Gd_2Zr_{1.2}Ce_{0.8}O_7$	Fluorite	0.53449	90	0.15269
$Gd_2Zr_{1.0}Ce_{1.0}O_7$	Fluorite	0.53643	90	0.15436
$Gd_2Zr_{0.8}Ce_{1.2}O_7$	Fluorite	0.53817	90	0.15587
$Gd_2Zr_{0.6}Ce_{1.4}O_7$	Fluorite	0.53953	90	0.15705
$Gd_2Zr_{0.4}Ce_{1.6}O_7$	Fluorite	0.54103	90	0.15837
$Gd_2Zr_{0.2}Ce_{1.8}O_7$	Fluorite	0.54183	90	0.15907
$Gd_2Ce_2O_7$	Fluorite	0.54300	90	0.16010

Table 2. Phase structure and lattice parameter *a* and cell volume of $Gd_2Zr_2O_7$ samples irradiated with 2 MeV Xe^{20+} ions at various fulences

Sample	Fluence (ions/cm^2)	Phase	*a* (nm)	*α* (°)	*V* (nm^3)
PDF00-016-0799	——	Pyrochlore	1.05010	90	1.15796
$Gd_2Zr_2O_7$	——	Pyrochlore	1.05231	90	1.16528
1	1×10^{13}	Pyrochlore	1.05287	90	1.16714
2	1×10^{14}	Pyrochlore	1.05360	90	1.16957
3	1×10^{15}	Pyrochlore	1.05364	90	1.16971
4	1×10^{16}	Pyrochlore	1.05397	90	1.17080

Table 3. Phase structure and lattice parameter a and cell volume of $Gd_2Ce_2O_7$ samples irradiated with 2 MeV Xe^{20+} ions at various fulences

Sample	Fluence (ions/cm^2)	Phase	a (nm)	α (°)	V (nm^3)
PDF01-080-0471	——	Fluorite	0.52636	90	0.14583
$Gd_2Ce_2O_7$	——	Fluorite	0.54197	90	0.15919
1	1×10^{13}	Fluorite	0.54219	90	0.15939
2	1×10^{14}	Fluorite	0.54300	90	0.16010
3	1×10^{15}	Fluorite	0.54378	90	0.16079
4	1×10^{16}	Fluorite	0.54627	90	0.16301

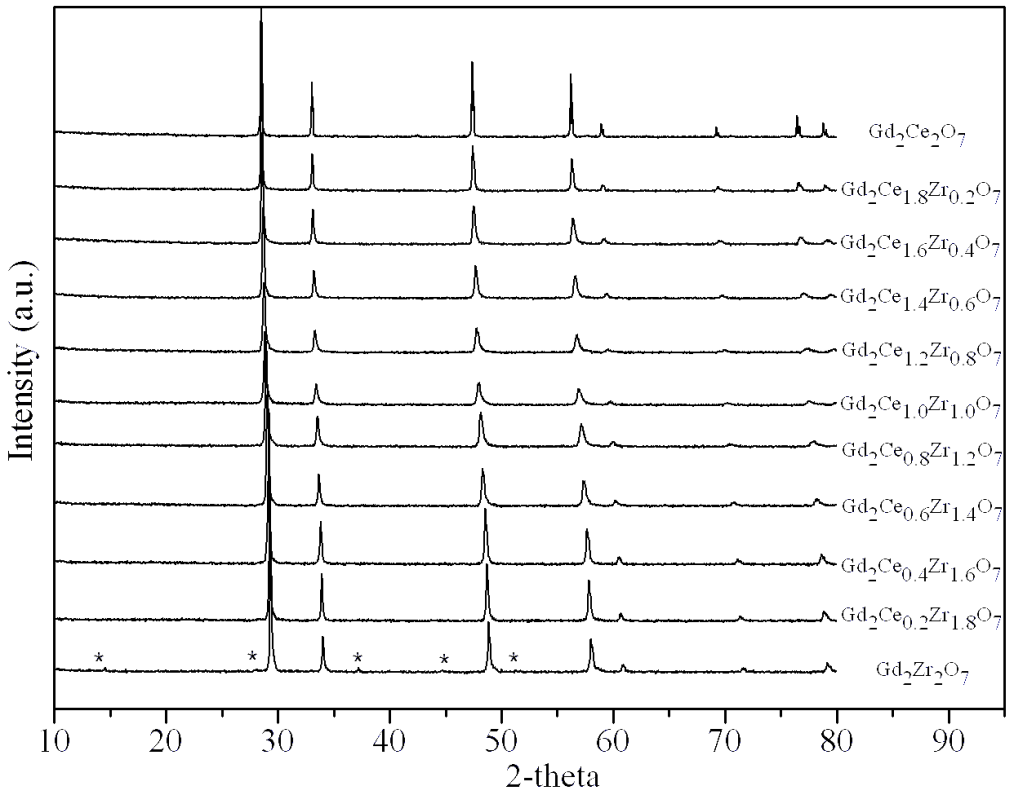

Fig. 1. XRD patterns of some of the compositions in $Gd_2Ce_xZr_{2-x}O_7$. The peaks corresponding to the supercell of the pyrochlore structure are noted with a star.

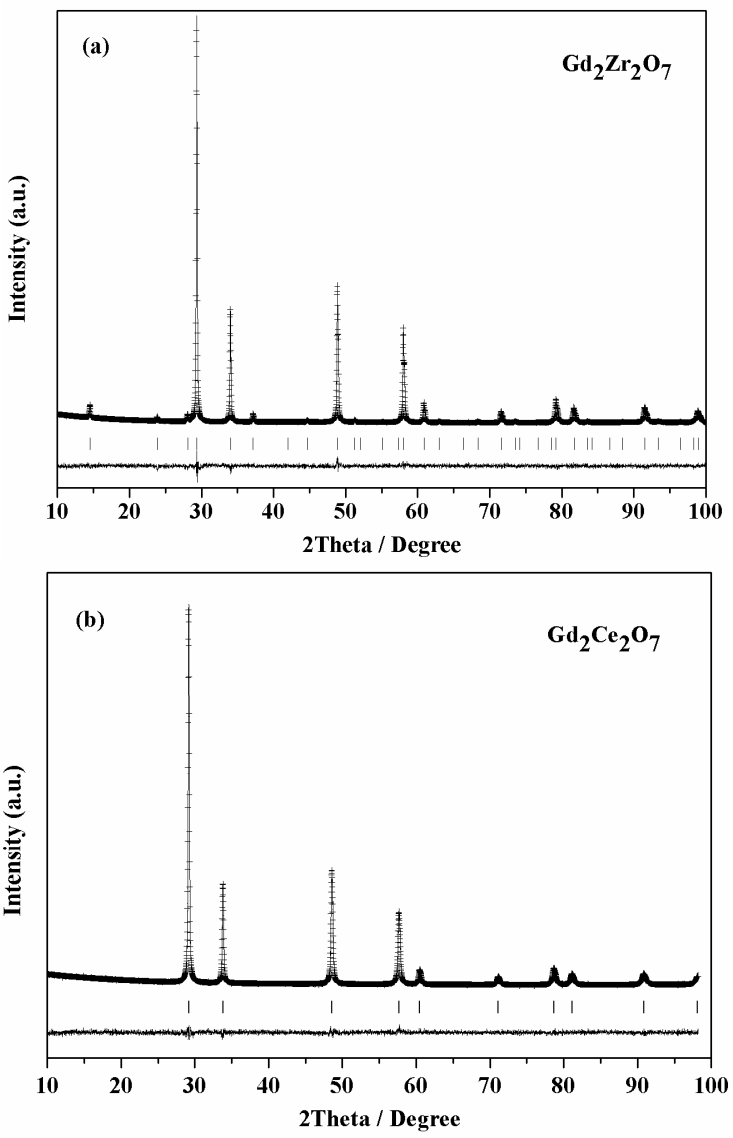

Fig. 2. Rietveld refinement results of powder X-ray diffraction of (a) $Gd_2Zr_2O_7$ and (b) $Gd_2Ce_2O_7$.

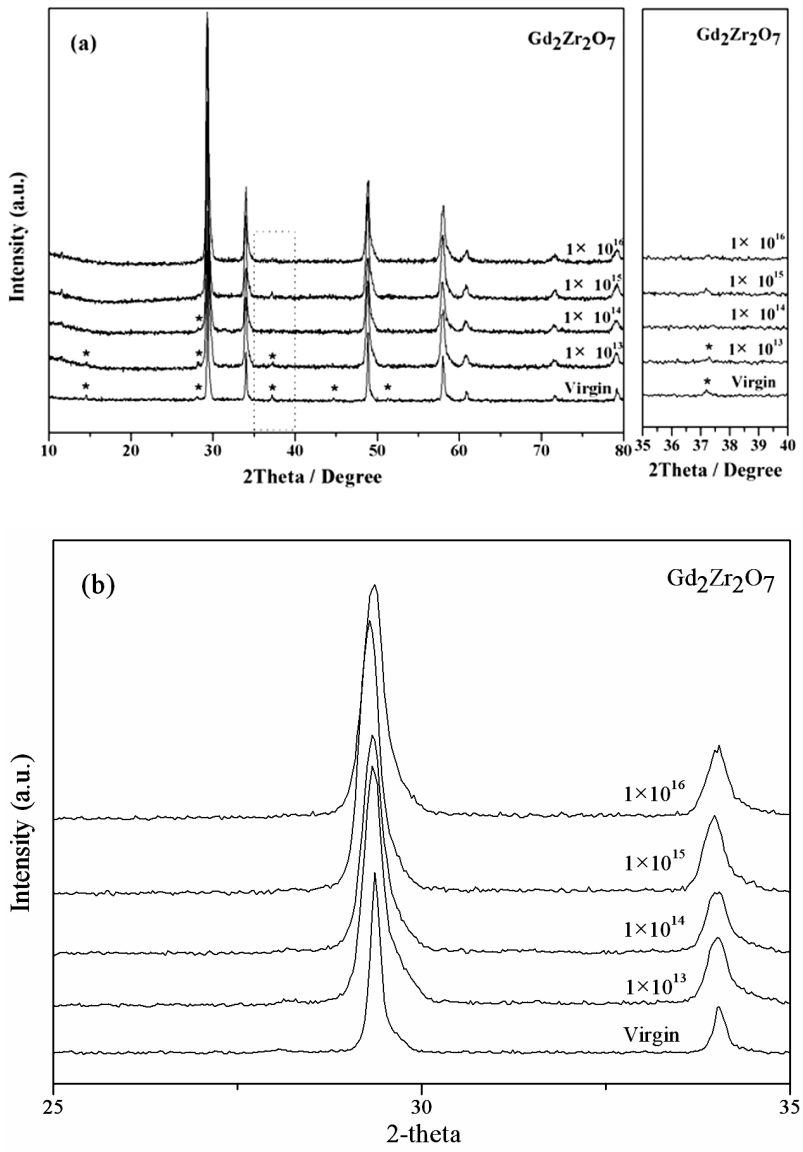

Fig. 3. (a) Evolution with the ion fluence of XRD patterns of $Gd_2Zr_2O_7$ irradiated with 2 MeV Xe^{20+} ions; (b) zoom of the 25-35° region. The peaks corresponding to the supercell of the pyrochlore structure are noted with a star.

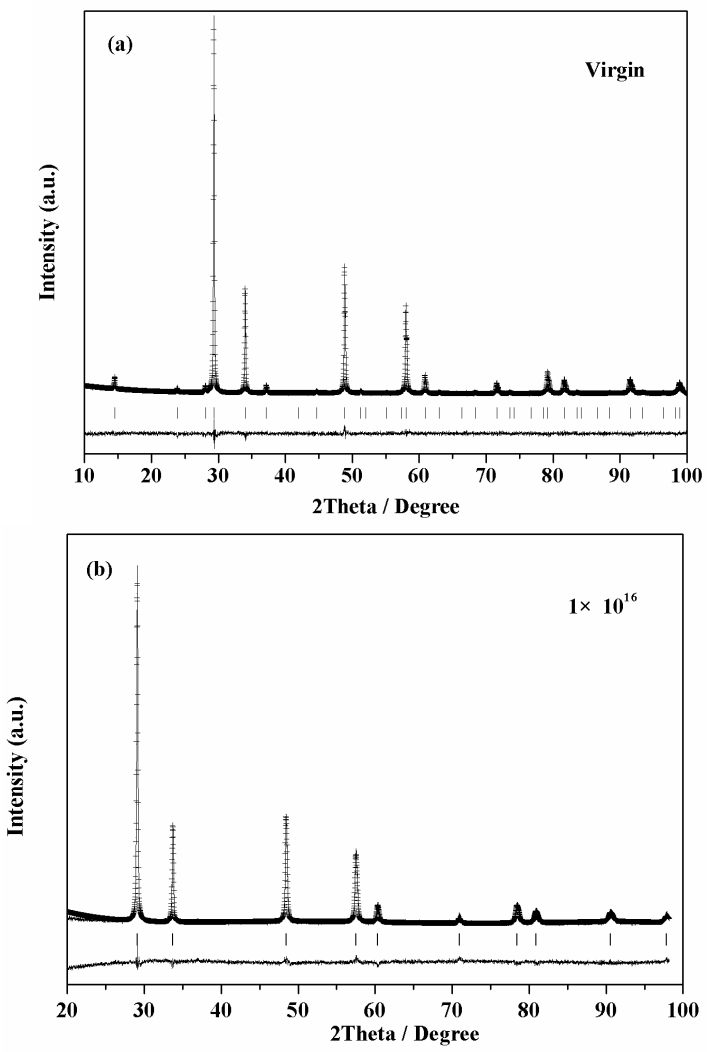

Fig. 4. Rietveld refinement results of powder X-ray diffraction of $Gd_2Zr_2O_7$ (a) virgin and (b) irradiated with 2 MeV Xe^{20+} at fluences of 1 × 10^{16} ions/cm^2

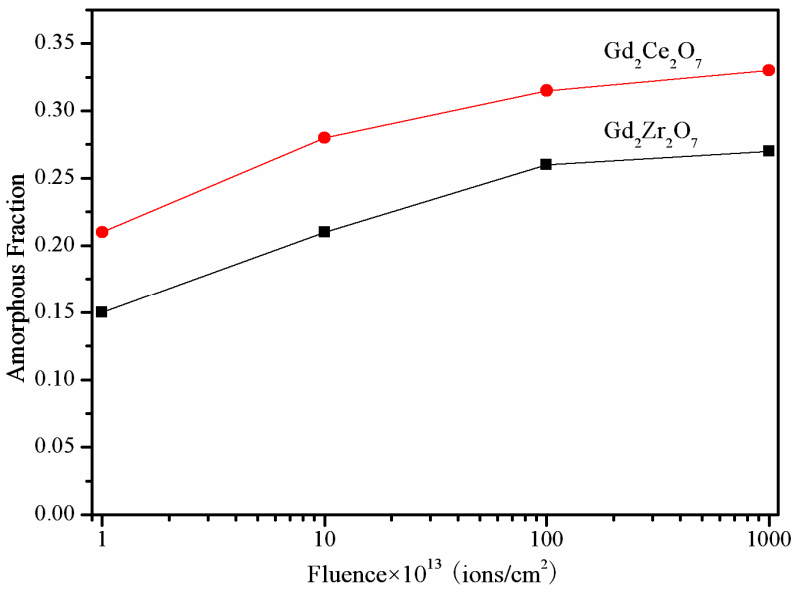

Fig. 5. Relative amorphous fraction of the samples irradiated at various fluences

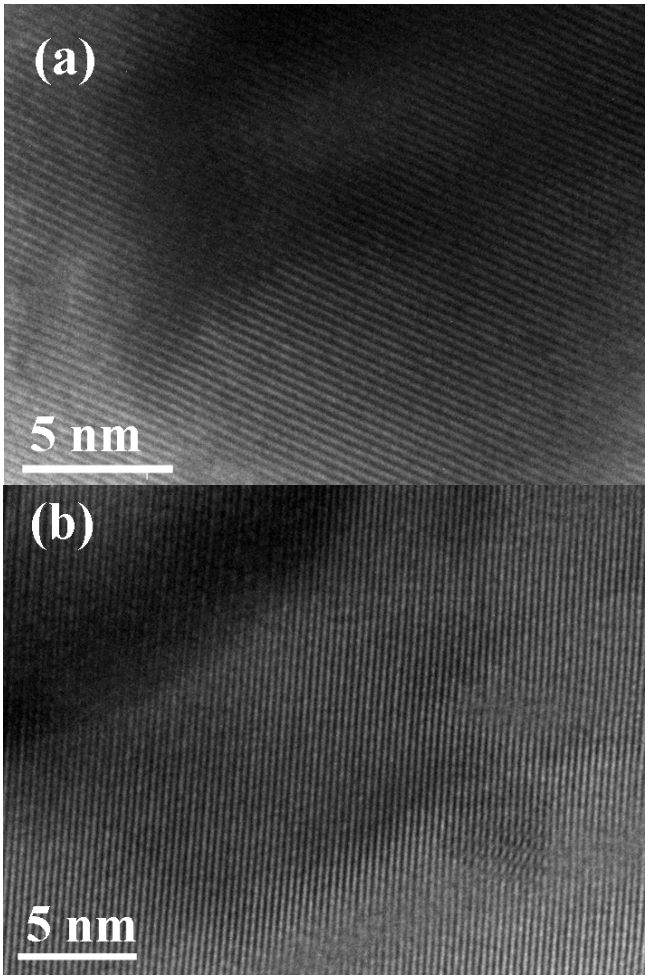

Fig. 6. HRTEM images of $Gd_2Zr_2O_7$ irradiated by 2 MeV Xe^{20+} ions at different fluences: (a) unirradiated; (b) 1×10^{16} ions/cm^2

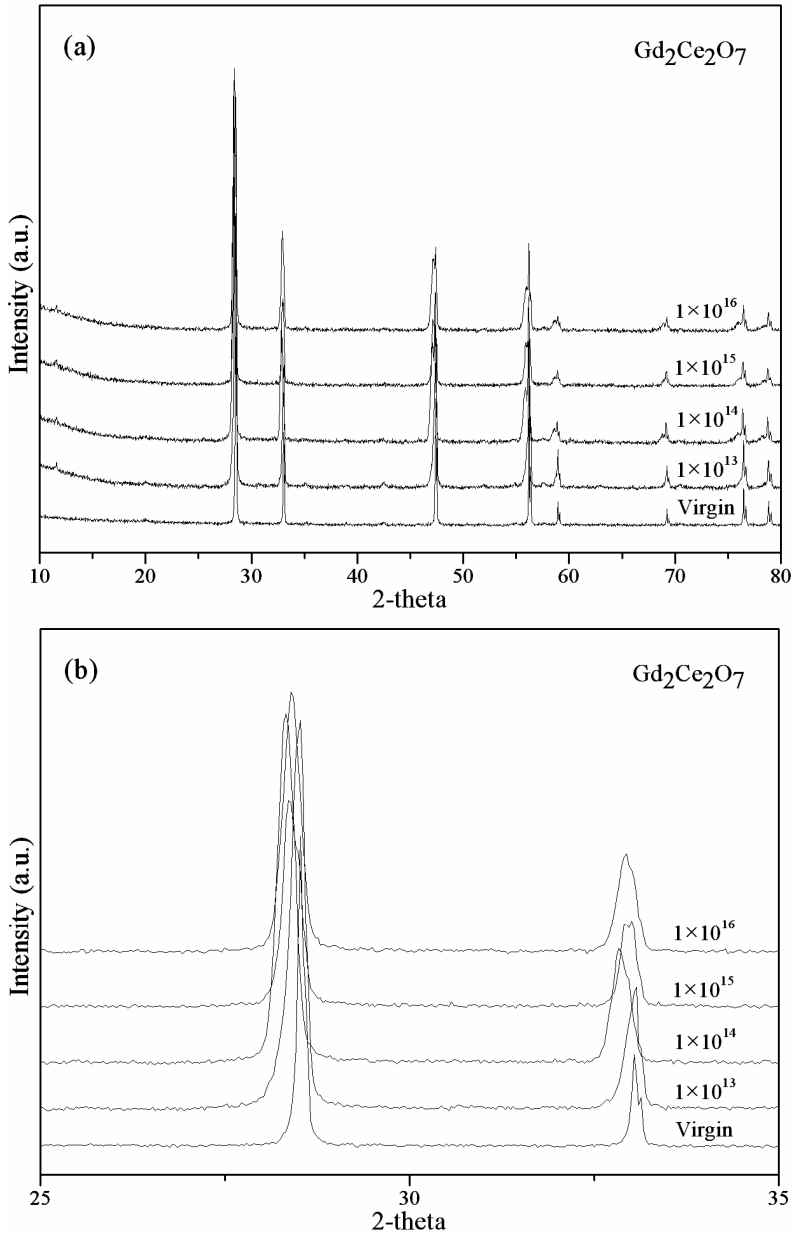

Fig. 7. (a) Evolution with the ion fluence of XRD patterns of $Gd_2Ce_2O_7$ irradiated with 2 MeV Xe^{20+} ions; (b) zoom of the 25-35° region.

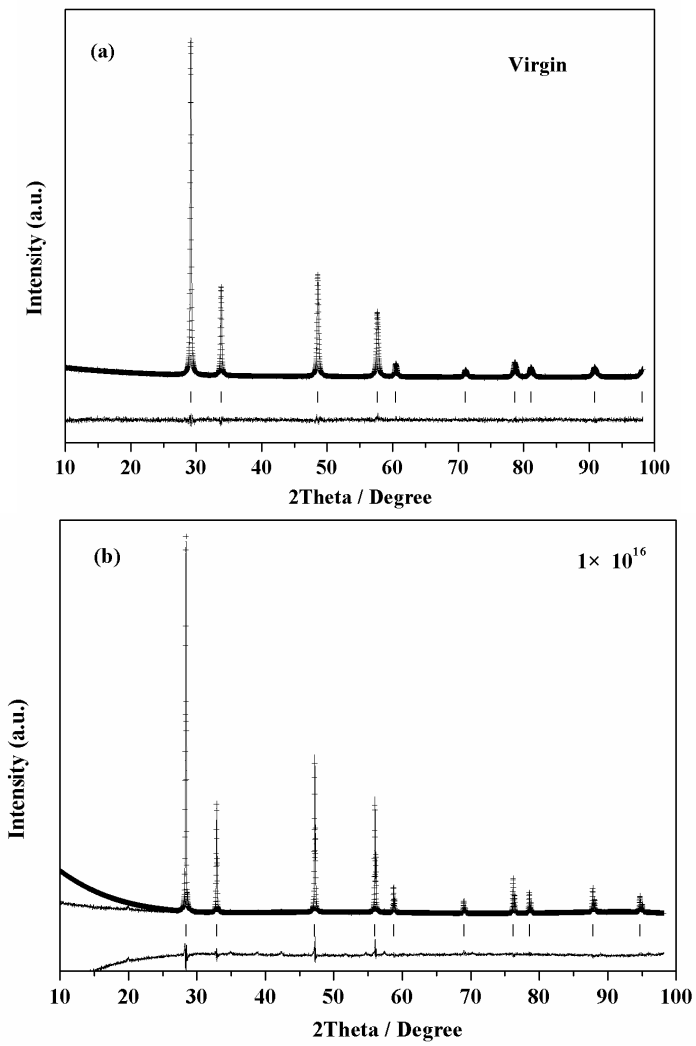

Fig. 8. Rietveld refinement results of powder X-ray diffraction of $Gd_2Ce_2O_7$ (a) virgin and (b) irradiated with 2 MeV Xe^{20+} at fluences of 1×10^{16} ions/cm^2

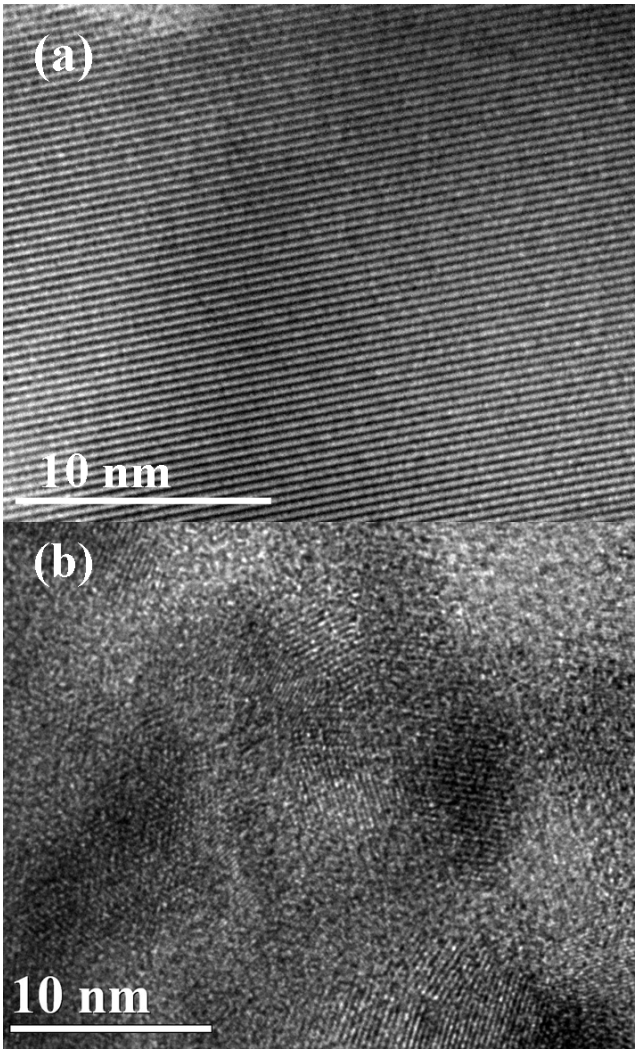

Fig. 9. HRTEM images of $Gd_2Ce_2O_7$ irradiated by 2 MeV Xe^{20+} ions at different fluences: (a) unirradiated; (b) 1×10^{16} ions/cm^2

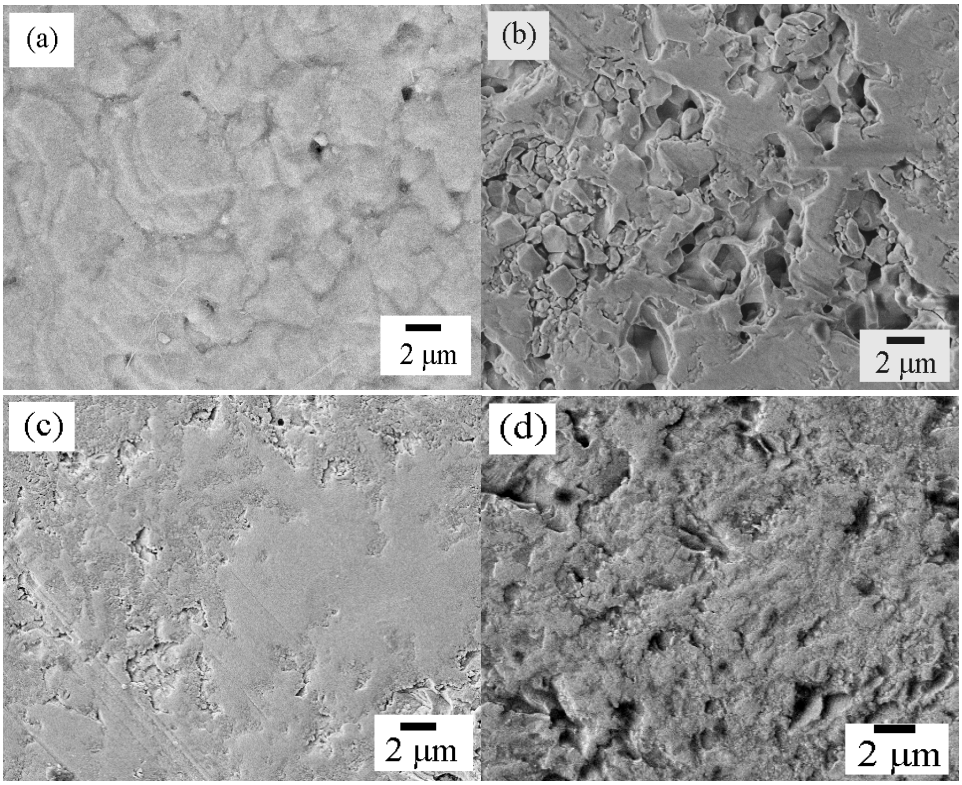

Fig. 10. SEM images of samples: (a) $Gd_2Zr_2O_7$ and (c) $Gd_2Ce_2O_7$ unirradiated; (b) $Gd_2Zr_2O_7$ and (d) $Gd_2Ce_2O_7$ irradiated with 2 MeV Xe^{20+} at fluences of 1×10^{16} ions/cm^2